CrossMark

Characterization of the crossover from capillary invasion to viscous fingering to fracturing during drainage in a vertical 2D porous medium

Amina Islam [a], Sylvie Chevalier [a], Imen Ben Salem [a], Yves Bernabe [b], Ruben Juanes [b], Mohamed Sassi [a,*]

[a] Masdar Institute of Science and Technology, P.O. Box 54224, Abu Dhabi, United Arab Emirates
[b] Massachusetts Institute of Technology, 77 Massachusetts Avenue, Building 48, Cambridge, MA 02139, USA

ABSTRACT

We experimentally studied the displacement of a viscous wetting fluid (water) by an inviscid non-wetting fluid (air) injected at the bottom of a vertical Hele-Shaw cell filled with glass microbeads. In order to cover a wide parameter space, the permeability of the porous medium was varied by using different bead size ranges and diverse air flow rates were generated by means of a syringe pump. A LED light table was used to back illuminate the experimental cell, allowing a high speed camera to capture images of the drainage process at equal time intervals. The invasion occurred in intermittent bursts. Image processing of the bursts and fractal analysis showed successive transitions from capillary invasion to viscous fingering to fracturing during the same experiment, dependent on the medium permeability, the air injection flow rate, and the vertical position in the cell. The interplay between the capillary, viscous and gravity forces determines the nature of the invasion pattern and the transitions, from capillary invasion to viscous fingering with decreasing fluid pressure on one hand and from viscous fingering to fracturing with decreasing effective overburden pressure on the other hand.

© 2013 Elsevier Ltd. All rights reserved.

1. Introduction

With the increasing global concern of anthropogenic CO_2 contributing to global warming, carbon capture and storage (CCS) is seen as a possible method of mitigating atmospheric CO_2 (IPCC Special Report on Carbon Capture and Storage, 2005). Deep saline aquifers are identified as having a high potential global capacity for long-term CO_2 storage. The potential of these reservoirs is particularly attractive in countries where depleted oil reservoirs are not available in the short term. Injection of CO_2 into saline aquifers involves the immiscible displacement of a viscous wetting phase (brine) by an inviscid non-wetting phase (CO_2), a process known as drainage.

Historically, drainage in porous media has been experimentally studied in Hele-Shaw cells for the concern of petroleum engineering. Experiments involved two liquids of different physical properties, radial or linear flows, miscible or immiscible fluids and different configurations of the cells. Interesting results could be found in various previous works (Saffman and Taylor, 1958; Smirnov et al., 2005; Homsy, 1987; Kopf-Sill and Homsy, 1988; Jiao and Maxworthy, 2008). For instance, Saffman and Taylor (1958) did experiments in Hele-Shaw cells to show how viscous fingering occurs when a less viscous fluid displaces a more viscous fluid. They

developed a theory to show the criteria for stabilizing and destabilizing the interface between two fluids and how it depends on the differences in density, viscosity and surface tension. However, their theory does not take into account the variations in capillary pressure or viscous forces at the pore scale of heterogeneous porous media. Kopf-Sill and Homsy (1988) characterized the range of length scales associated with tip splitting. They observed that the tip velocity to be approximately constant regardless of the occurrence of splitting events, and the average finger width decreased as the modified capillary number increased. Smirnov et al. (2005) did microgravity experiments of linearly injected dyed-water into a horizontal Hele-Shall cell saturated by a water–glycerine solution. They varied the thickness of the cell, the injection flow and the viscosity ratio between fluids to obtain images of the different flow regimes. Jiao and Maxworthy (2008) performed experimental study of miscible displacements under the coupled effects of viscosity-contrast and gravity segregation and showed how the global displacement properties depended on the Gravity number and the Peclet number.

In this work, we focus on drainage caused by gas injection into a vertical, water saturated Hele-Shaw cell filled with glass beads, a geometry meant to represent CO_2 injection from a horizontal well into a saline aquifer.

It is essential to understand the transport of CO_2 into saline aquifers since the amount of CO_2 that can be injected and stored underground, is controlled by it. During the injection process

different flow regimes may occur. At the pore scale, the pore throats control the hydraulic conductance between the pore bodies initially saturated with the aqueous brine phase. The competition between the pressure gradients that drive viscous flow and the pressure jumps between immiscible fluids represented by the capillary pressure determine whether the invasion occurs under the capillary invasion regime or the viscous fingering regime (Løvoll et al., 2005). In the case where capillary pressureovercomes the pressure gradient that drives viscous flow, the injected non-wetting fluid moves through the largest pores (Zhang et al., 2011) and capillary invasion is observed. The invasion pattern consists then of broad, relatively homogeneous clusters. This invasion regime leads to efficient storage within the porous matrix. However, when viscous forces in the pore throats prevail, the invading gas experiences preferential flow and long, thin viscous fingers are formed (Løvoll et al., 2005). The initiation of viscous fingering causes the CO_2 to invade only a fraction of the porous medium available for storage. Furthermore, low permeability of the porous medium or other flow barriers within the medium means that the desired flow rate could only be achieved by higher pressure gradient, which could result in fracturing of the rock matrix. The occurrence of fractures could result in the escape of the CO_2 gas to the surface, decreasing storage efficiency and compromising the viability of storage (Holloway, 2005).

To acquire a thorough understanding of the crossover from capillary invasion to viscous fingering to fracturing during drainage, we conducted experiments using fast imaging visualization of the phenomena. We used a vertical 2D configuration in order to simulate drainage during CO_2 injection from a horizontal well (Fig. 1a and b) since this is the best arrangement to increase CO_2 contact with brine and to optimize CO_2 storage capacity (Ghaderi et al., 2009). This configuration is comparable to a single injection point in the center of the bottom side of a vertical Hele-Shaw cell such as the one used in the present study (Fig. 1c). Fast images of the gas invasion patterns were acquired during the injection of air into the water-saturated porous medium (consisting of glass microbeads) at atmospheric pressure and laboratory temperature.

Drainage experiments in Hele-Shaw cells have been previously reported in the literature. Løvoll et al. (2005) studied the competition between capillary, viscous and gravity forces on the flow regimes in random porous media. The type of displacement occurring during these drainage experiments was governed by the relative magnitude of the viscous and gravity forces with respect to the capillary forces. These relative magnitudes can be quantified through two dimensionless numbers: the capillary number Ca (viscous pressure drop at pore scale to the capillary pressure) and the Bond number Bo (hydrostatic pressure drop over a pore to the capillary pressure).

$$Ca = \frac{\nabla p_{viscous}}{\nabla p_{cap}}$$

$$B_o = \frac{\nabla p_{grav}}{\nabla p_{cap}}$$

In absence of gravity effects, whether the flow regime is capillary invasion or viscous fingering is solely controlled by the capillary number. For slow flow rates, the capillary forces govern the displacements and the invasion is guided by the capillary pressure, i.e., the difference between the gas and brine pressures along their interface. As the capillary pressure decreases with increasing pore size, the larger pores are more easily invaded. Drainage is therefore controlled by the spatial distribution of pore sizes. As the invasion flow rate is increased, viscous forces overcome the capillary forces leading to the destabilization of the interface. This destabilizing effect results in the formation of invasion fingers. While viscous forces have a destabilizing effect on the flow regimes, gravity has a stabilizing one (Løvoll et al., 2005). However even in the presence of gravity, viscous forces dominate in the case of fast displacements and viscous fingering is observed. Løvoll et al. (2005) experimentally determined the threshold for instability but they used an experimental configuration inconsistent with the injection of CO_2 in saline aquifers as illustrated in Fig. 1. They extracted the aqueous phase from the bottom outlet of the Hele-Shaw cell, letting air invade the porous medium through the top inlet. The Hele-Shaw cell could be tilted to vary the gravity effect.

Another significant characteristic of the drainage process is the episodic nature of the displacement. Air displaces the water by a succession of irregular bursts. This phenomenon was observed in translucent Hele-Shaw experiments by Crandall et al. (2009).
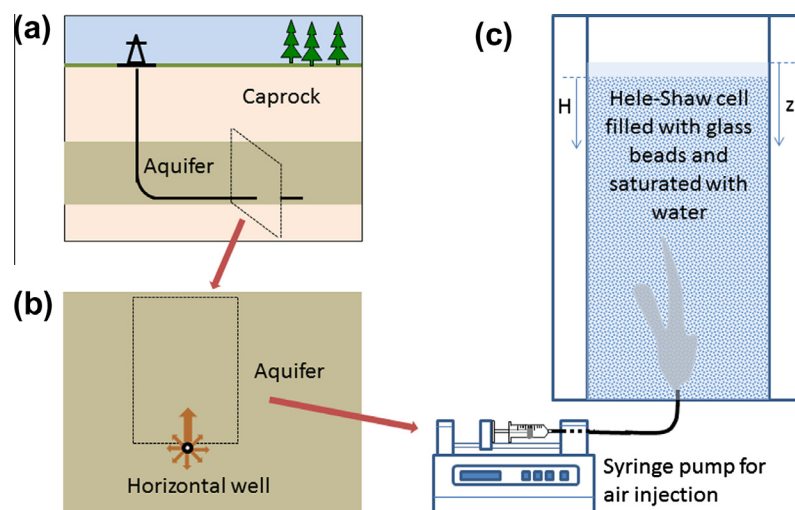

Fig. 1. (a) CO_2 injection through a horizontal well into a saline aquifer; (b) a vertical cross-section of the well is isolated to define the conceptual model of the 2D experiments; (c) phenomenon is represented by drainage in a vertical water-saturated Hele-Shaw cell filled with glass beads with a single injection point of gas at the bottom center.

When the air injection begins, invasion does not occur immediately. The air pressure must first exceed the capillary entry pressure. At this point, the pressure is sufficiently large to allow invasion of several pores simultaneously. Air pressure tends to drop off as the invaded pore volume increases and the water pressure increases locally at the interface in response to the invading air, contributing to stop the invasion (Holtzman and Juanes, 2010). Further invasion is suppressed until air pressure builds up again due to the continuous air injection and local water pressure dissipates (Holtzman and Juanes, 2010). Then a new burst cycle could occur. Crandall et al. (2009) extensively studied this burst phenomenon using a configuration quite similar to ours. They analyzed the occurrence, size and distribution of bursts during drainage experiments but restricted their investigation to the capillary flow regime by using low injection rates. They also only performed horizontal experiments to avoid any gravity effect and injected air linearly on one side of the cell. Furthermore they used a throat network directly fashioned within the cell representing a non-deformable porous media.

Neither of these previous works took into account both the fracturing phenomenon represented by solid particle displacements and the effect of gravity in a vertical Hele-Shaw cell. As gas pressure increases, a fracture can form if cohesive and overburden forces are overcome by the capillary forces. In a granular medium, the onset of fracturing depends on the competition between the resisting inter-particle forces and the hydrodynamic forces that promote pore opening. In a vertical system, the viscous fingering regime can turn into fracturing as air ascends and the overburden forces decrease. Fauria and Rempel (2011) experimentally studied the phenomena. They conducted invasion experiments through a vertical sand layer while monitoring the overpressure up to the gas breakthrough. A transition from capillary invasion to fracture-dominated invasion is identified when gas invasion is observed before the capillary-controlled overpressure is reached. Comparing the threshold overpressures for initial gas invasion using different particle sizes, their experiments confirmed that the invasion was controlled by capillary forces when the overburden effective stress applied at particle contacts was sufficiently large. At lower effective stresses they observed a fracture-dominated invasion. However their experiments did not allow visualizing the transition from capillary invasion to viscous fingering. The dynamics of the invasion could not be visualized as well and no image analysis procedures were performed. Holtzman and Juanes (2010) and Holtzman et al. (2012) studied numerically and experimentally the crossover from fingering to fracturing in deformable media. However they performed air injection into a thin bed of water-saturated glass beads packed in a horizontal circular cell. Gravity therefore played no role but a vertical confining weight was applied on the horizontal porous medium simulating an overburden stress on the particles. The intermittent propagation of air during the fingering flow regimes was observed but in fracturing regime air advanced continuously. The different regimes were identified through fractal analysis of the invasion images. They numerically established a phase diagram showing the three invasion regimes as a function of two dimensionless numbers: a modified capillary number (to take into account the pore distribution) and a fracturing number (i.e., the ratio of the pressure force increment after drainage of a pore to the force increment resulting from deformation). Furthermore, they analyzed the effect of the degree of randomness of the media on the flow regime.

In this work, we experimentally studied the transition from capillary invasion to viscous fingering to fracturing during drainage resulting from air injection in a water-saturated, vertical Hele-Shaw cell filled up with a deformable porous medium. Air was introduced through a single injection point at the bottom of the cell. Our experimental system allowed visualization and image analysis of the three different flow regimes. The dynamics of the invasion were also investigated. The effect of gravity was taken into consideration in our analysis.

2. Experimental setup

The experimental set up for the drainage experiments is shown in Fig. 2. We constructed Hele-Shaw cells with standard glass plates, 300 mm by 200 mm in size. Two plates were positioned parallel to each other, separated by pencil leads along three borders and sealed in place with silicon. The precise diameter of pencil leads ensured the uniformity of the gap between the plates. Two diameters of pencil leads were used, 1 and 2 mm. The cells were sealed by silicon on three sides while the top was left open to enable the invading air to escape. Before completely sealing the bottom, a G20 hypodermic needle for the gas injection was installed vertically at the center between the two plates. The needle had an internal diameter of 0.686 mm. The cells were tightly packed with glass microbeads and shaken to ensure uniform packing. Two sets of glass microbeads were utilized: (a) 0.32–0.43 mm and (b) 0.57–0.70 mm.

Air was injected at a constant flow rate using a syringe pump (NE-4000) from the single entry point at the center bottom of the Hele-Shaw cell. Air was used instead of CO_2 for practical reasons. However, at atmospheric pressure and room temperature, air and CO_2 have similar properties as shown in Table 1.

The invasion patterns corresponding to different injection flow rates were visualized for the two sets of glass beads. Snapshots were captured at 0.1 s intervals using a CCD camera (Sony XCL 5005CR CCD Camera) directly connected to the computer through the PIXCI Imaging board (Sony Inc.). To ensure uniform illumination of the Hele-Shaw cell, we used a LED Light Table positioned behind the cell. An advanced image processing software called
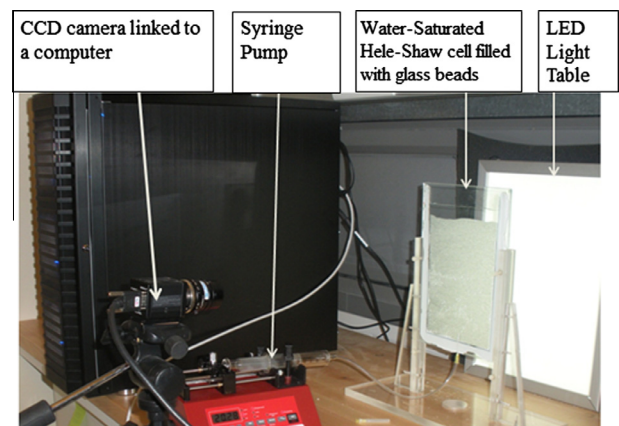

Fig. 2. Experimental set up to visualize the drainage invasion patterns.

Table 1
Properties of air and CO_2 at temperature = 298 K, and P = 1 bar (Lemmon et al., 2007; Chun and Wilkinson, 1995).

	CO_2	Air
Density (kg/m^3)	1.79	1.17
Interfacial tension (mN/m)	71.03	72
Viscosity (μ Pa s)	14.9	18.4

XCAP^{TM} software (EPIX Inc.) was used for post-capture image enhancement and invasion pattern analysis.

3. Methodology

3.1. Estimation of experimental parameters

In this section we give the details of how the experimental parameters such as porosity, permeability, capillary number and flow velocity were determined. For each of the two different glass microbead sizes used, the porosity and permeability values are presented in Table 2. The injection rate was also varied between experiments leading to different reference velocities as summarized in Table 3.

To evaluate the porosity, microbeads were packed within a Hele-shaw cell filled with a known volume of water (V_1). The volume in the cell up to the microbeads level was noted (V_2). The volume in the cell up to water free surface was recorded (V_3). The volume of fluid displaced gives the volume of the immersed microbeads without the pores (V_b) and is calculated using Eq. (1). The porosity φ is then given by Eq. (2). It should be noted that the free water level is higher than the packed microbeads level in the cell as shown in Figs. 1 and 2.

$$V_b = V_3 - V_1 \tag{1}$$

$$\text{Porosity}\,\varphi = 1 - \frac{V_b}{V_2} \tag{2}$$

Since glass microbeads of different sizes were inserted in the Hele-shaw cells to simulate a real porous medium, permeability values were calculated using Eq. (3) below, from Mota et al. (2001), where φ is porosity, d_p is the particle diameter (m), τ is tortuosity and K_0 is a shape factor equal to 2.

$$k = \left(\frac{\varphi}{\tau}\right)^2 \left(\frac{\varphi d_p^2}{36(1-\varphi)^2 K_0}\right) \tag{3}$$

The tortuosity was approximated using the following equation (Mota et al., 2001).

$$\tau = \frac{1}{\varphi^{0.4}} \tag{4}$$

As described previously the capillary number is a dimensionless number devised for quantifying the ratio of viscous forces to capillary forces. It is defined by Eq. (5), where σ (N/m) is the surface tension, μ_l (Pa s) the viscosity of the displaced fluid (water), v (m/s) the velocity of the invading fluid (air), d_{av} the average bead size (m) and k_{av} the average permeability (m^2).

$$Ca = \frac{\mu_l v \left(\frac{d_{av}}{6}\right)^2}{\sigma k_{av}} \tag{5}$$

At the injection point, the flow velocity is computed from Q (m^3/s), the volumetric flow rate, A_c (m^2) the cross-sectional area

Table 3
Velocities and capillary numbers at the injection point for the different injection rates studied for each set of microbead sizes.

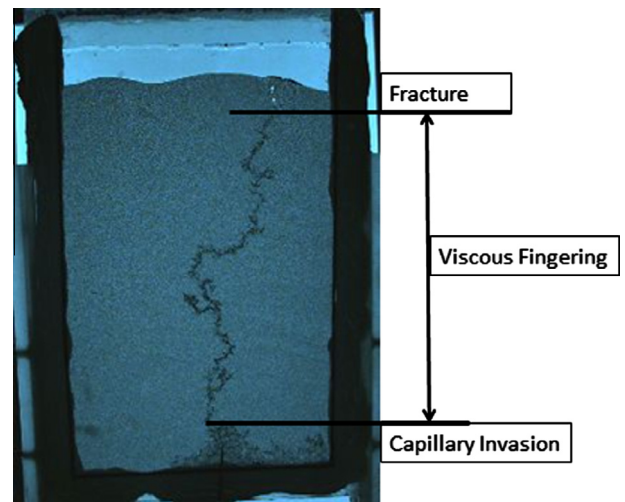| Flowrate (mL/min)	Gap between the glass plates (mm)	Capillary number
Bead size 0.57–0.70 mm		
2	2	2.87×10^{-4}
4	2	5.74×10^{-4}
8	2	11.5×10^{-4}
20	1	28.7×10^{-4}
Bead size 0.32–0.43 mm		
3.4	2	4.83×10^{-4}
4	2	5.68×10^{-4}
8	2	11.4×10^{-4}
Bead size 0.43–0.57 mm		
3.8 mL/min	2	5.38×10^{-4}

Fig. 3. Invasion for a Hele-Shaw cell with 0.32–0.43 mm beads at an injection rate of 3.4 mL/min showing the transition from capillary invasion to viscous fingering to fracturing.
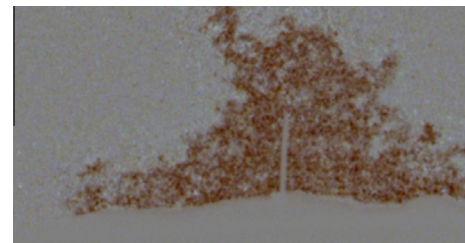

Fig. 4. Experimental image from XCAP^{TM} after subtracting the background image.

of the injection needle, and D (m) the diameter of the injection needle using the following equation.

$$v = \frac{Q}{A_c} = \frac{4Q}{\pi D^2} \tag{6}$$

Table 2
Porosity and permeability values for each set of microbeads sizes.

Bead size (mm)	0.57–0.70	0.43–0.57	0.32–0.43	0.1–0.2
Porosity	0.45	0.45	0.45	0.44
Permeability (m^2)	$7.18 \times 10^{-10} – 1.08 \times 10^{-9}$	$4.1 \times 10^{-10} – 7.2 \times 10^{-10}$	$2.26 \times 10^{-10} – 4.08 \times 10^{-10}$	$1.96 \times 10^{-11} – 7.8 \times 10^{-11}$

Fig. 5. Example of binarized image for capillary invasion.

Fig. 7. Plot for log (box size) vs. log (number of boxes containing foreground pixels) for the image of Fig. 6, showing fractal dimension number = 1.69 with r^2 = 0.9979 and standard deviation = 0.0668.

Since the glass microbeads are not consolidated, the effective overburden pressure at any given point on the solid phase is equal to the weight of the overlaying microbeads minus the buoyant force divided by the average projected area of microbeads and is given by Eq. (7), where ρ_s and ρ_l (kg/m^3) are respectively the solid (glass) and liquid (water) densities, g (m^2/s) is the acceleration of gravity, and H(m) the vertical distance from the top surface of the bead pack, as shown in Fig. 1.

The effective overburden pressure is:

$$\sigma_v \approx (\rho_s - \rho_l)g(1 - \varphi)H \tag{7}$$

The hydrostatic pressure is calculated using Eq. (8), where z (m) is the vertical distance from the top surface of the water.

$$\text{Hydrostatic pressure} \approx \rho_l g z \tag{8}$$

The glass microbeads are made of soda lime glass with a density of 2.5 g/cm^3 (Koike and Tomozawa, 2007).

3.2. Image processing and fractal dimension number

All acquired images were processed using XCAP™ (EPIX Inc.) in order to improve the visualization of the intermittent invasion processes. A background image was subtracted from the successive images. Notice however that, in the case of fracturing, the background image was subtracted in such a way that the void space left by the displaced solid particles was darkened instead of lightened as happened when air displaces water. As a consequence of our experimental configuration, the invasion pattern changed during the course of a single injection experiment. All three regimes (capillary invasion, viscous fingering and fracture) successively appeared within the same experiment. Hence, the image of the cell was divided within each experimental run into different regions so as to isolate the different invasion patterns as shown in Fig. 3. The image portions corresponding to different regimes were then analyzed separately. As an example, Fig. 4 shows a processed image of the capillary invasion regime.

The processed color images were converted to 8-bit binary images, as shown in Fig. 5, allowing computation of the fractal dimension 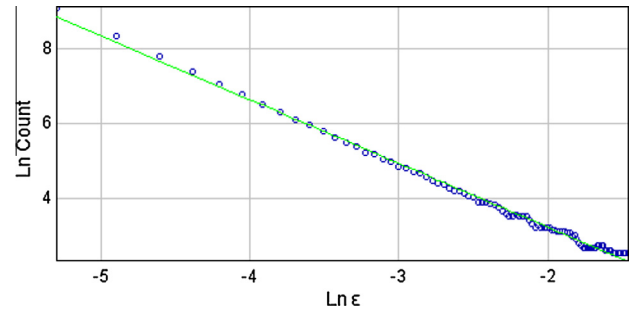of the invaded pore space using the standard box-counting method on Fraclab, a plug-in implemented in the image-processing freeware ImageJ (ImageJ). Fraclab and ImageJ were successfully used in previous studies to analyze similar kind of experimental results (Crandall et al., 2009). The fractal dimension is a measure of complexity calculated as the ratio of the change in detail of an image to the change in scale. In the box-counting method, the image is divided into boxes of decreasing sizes as shown in Fig. 6. For each box size ε, the number of boxes containing foreground pixels is counted. The fractal dimension number is the slope of the regression line in a log–log plot of box size (x axis) versus box count containing foreground (or black) pixels (y axis), as shown in Fig. 7 (ImageJ). The obtained fractal dimension numbers are different for the three invasion regimes and may be used to identify the invasion pattern corresponding to the bursts (Holtzman and Juanes, 2010).

4. Results

We present invasion patterns for four experimental runs that represent the investigated phenomena. The invasion pattern for each experimental run showed characteristics of either two or three of the different regimes: capillary invasion, viscous fingering or fracturing. Note that the identification of the displacement patterns was based on the visual appearance as well as the fractal dimension results presented in Section 5.2 below.

4.1. Case 1: 0.57–0.70 mm beads with injection rate = 2 mL/min

Fig. 8 shows 6 snap-shots of the invasion pattern for case 1. All three regimes, capillary invasion, viscous fingering and fracturing, occurred in different portions of the cell. It can be seen that gravity effects had a stabilizing effect, as suggested by the typical capillary invasion appearing on the lower left side of the cell, a region of high hydrostatic pressure and overburden stress. At the center of the cell a typical viscous finger was formed, indicating that viscous forces were overcoming capillary forces and gravity there. Finally, at 118 s, a fracture appeared at the upper left hand side of the cell. Analysis of the binarized images shows that 10% of the porous
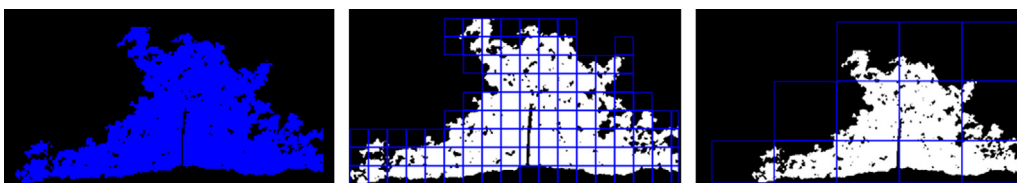

Fig. 6. Binary image divided into boxes (represented by blue grid) of decreasing size from left to right. (For interpretation of the references to colour in this figure legend, the reader is referred to the web version of this article.)
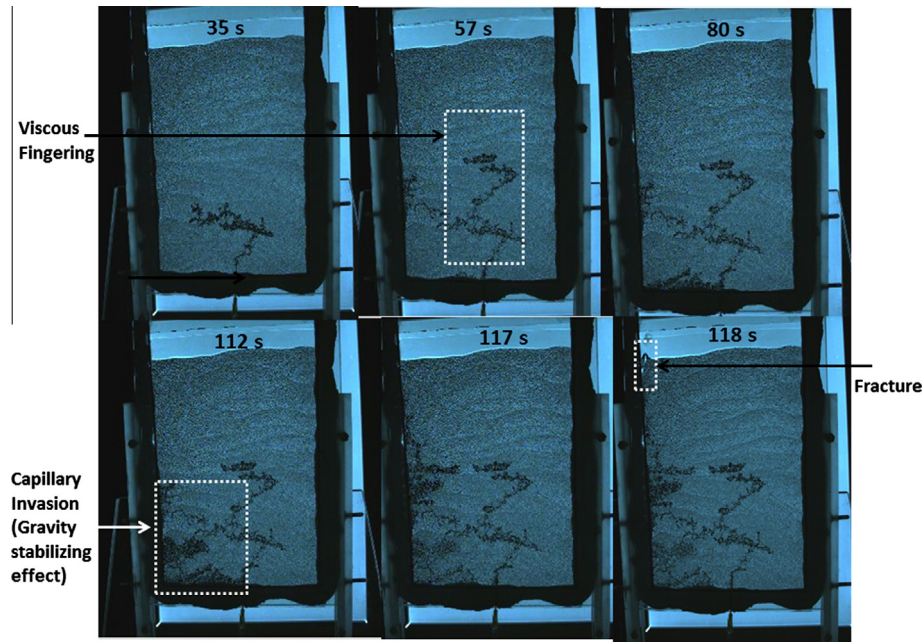
Fig. 8. Invasion pattern for 0.57–0.70 mm beads at air injection rate = 2 mL/min.

Table 4
Ratio of porous medium invaded by capillary invasion.

Case no.	Pixel count of capillary invasion	Pixel count of porous medium	Percentage of capillary invasion (%)
1	21429	212660	10.1
2	47734	1803459	2.6
3	17437	1186420	1.5

medium was invaded during the event of capillary invasion. This number was determined by calculating the ratio of pixels invaded during the capillary invasion to the number of pixels in the porous media as summarized in Table 4.

4.2. Case 2: 0.32–0.43 mm beads with injection rate = 3.4 mL/min

For case 2, the three regimes of invasion were also observed. As can be seen in Fig. 9, capillary invasion occurred at early times in the vicinity of the injection point. It was followed at 46.6 s by the formation of a viscous finger at a certain vertical distance from the injection point. As more air was injected, branching occurred along the main viscous finger. At 56.4 s a fracture opened near the top of the cell with clear evidence of displacement of the solid particles. Despite the air breakthrough at 56.4 s, subsequent injection resulted in similar fingering, branching and fracturing. For example, a viscous finger branched to the left at the upper part of the cell at 62.8 s probably due to the fact that the air pressure
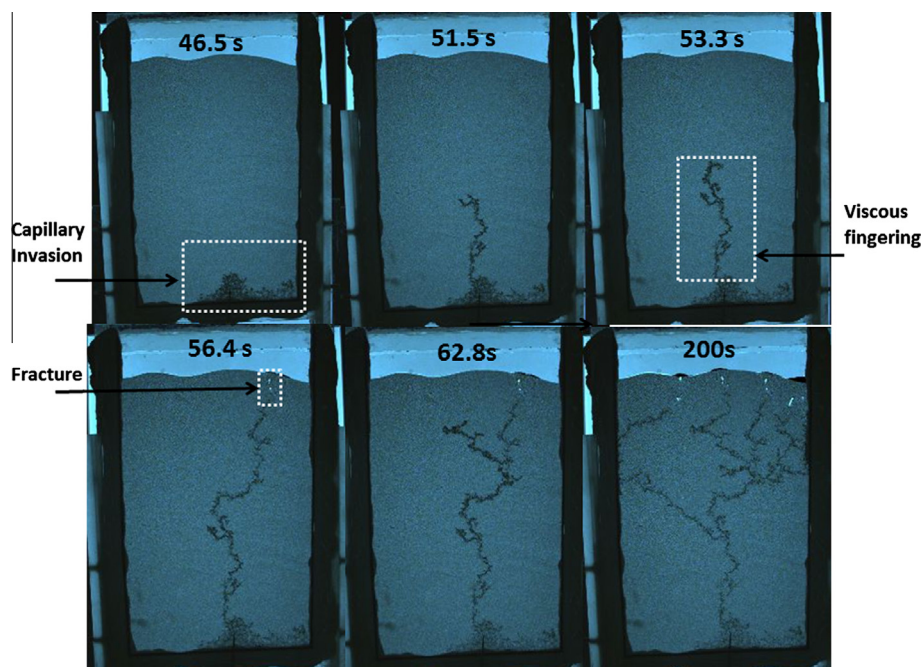

Fig. 9. Invasion pattern for 0.32–0.43 mm beads with injection rate = 3.4 mL/min.
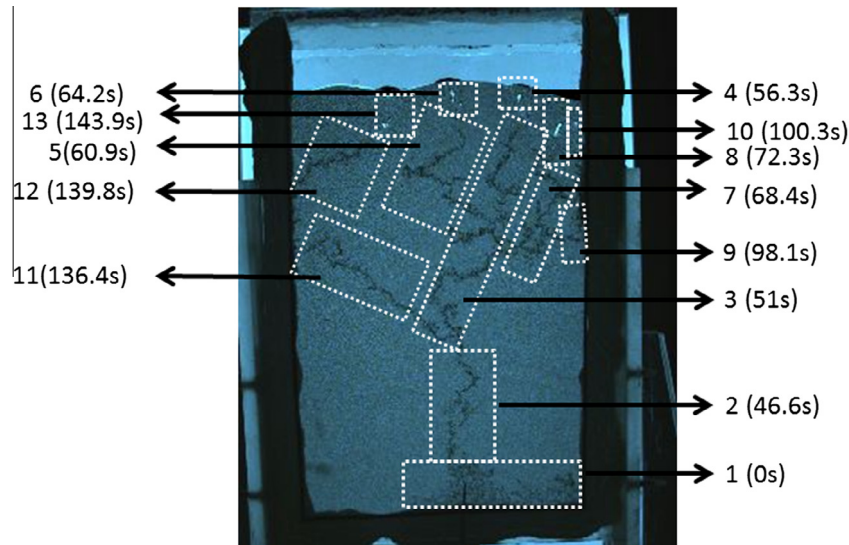
Fig. 10. The sequence of bursts, the time in brackets shows the time when the burst started.

decreased after the breakthrough at 56.4 s, allowing the water to reinvade the air channel. This in turn was followed by a new air pressure buildup in the lower half of the cell and the formation of a new viscous finger ending up in a fracture near the top of the cell. The entire cycle was repeated several times as seen on the 200 s snapshot of Fig. 9. Fig. 10 shows the sequence of bursts that lead to the final image of 200 s in Fig. 9. Note that all fracturing events appear approximately at the same height. Continuing the injection does not change the invasion pattern after 200 s. During this experiment, 2.6% of the porous medium was invaded by capillary invasion, a significantly lower percentage than that in case 1.

4.3. Case 3: 0.57–0.70 mm beads with injection rate = 8 mL/min

As in the previous cases, patterns of capillary invasion, viscous fingering and fracturing successively occurred within a single experiment (see Fig. 11). Capillary invasion was observed at 2 s, viscous fingers start to develop at the 4.5 s and a fracture can be seen towards the top of the left side of the cell at 6 s. The percentage of the porous medium that was invaded by capillary regime is only 1.5%, lower than Case 1 and 2. The air breakthrough occurred after only 8 s. Moreover only two branches develop instead of four in the lower velocity case presented in Section 4.2. Water was probably less capable to reinvade air channels after breakthrough.
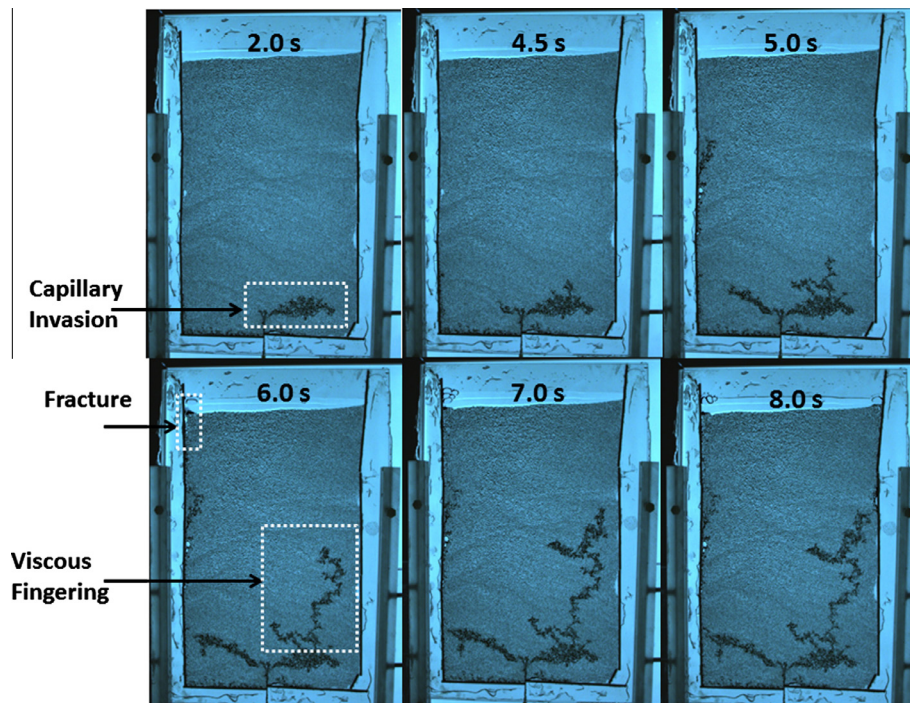

Fig. 11. Invasion pattern for 0.57–0.70 mm beads with injection rate = 8 mL/min.
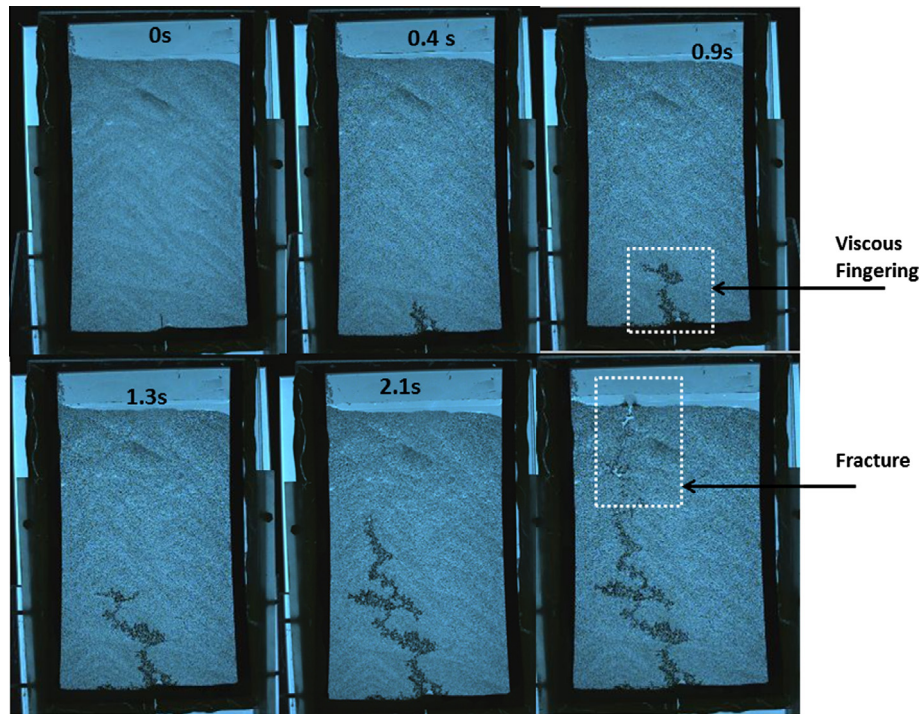
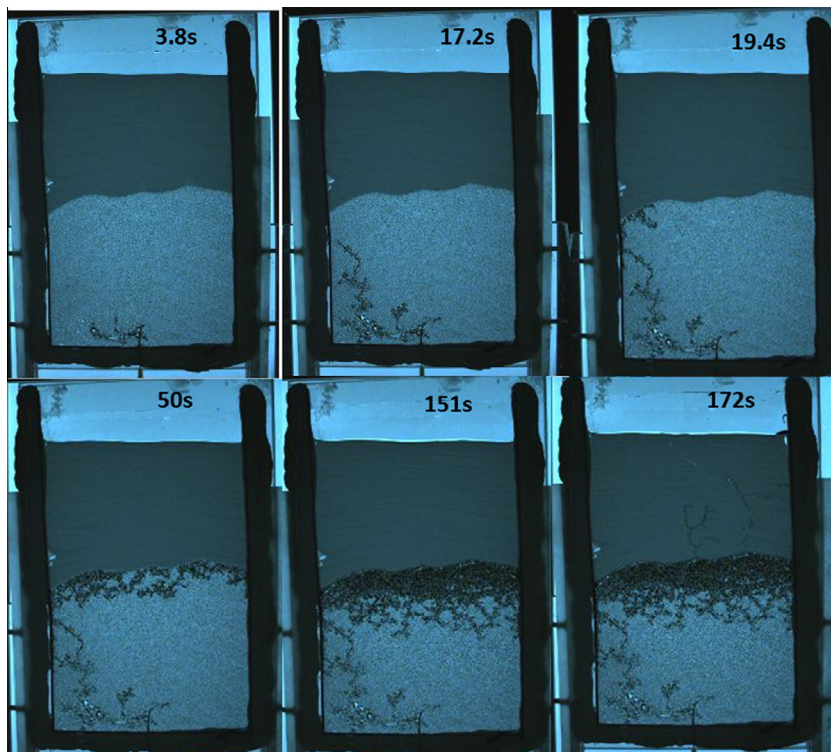**Fig. 12.** Viscous fingering and fracturing at 20 mL/min for 0.57–0.7 mm beads.

Fig. 13. Stratified porous media with air injected at 3.8 mL/min.

4.4. Case 4: 0.57–0.70 mm beads with injection rate = 20 mL/min

The invasion pattern can be seen in Fig. 12. Viscous finger-ing occurred from the start, followed by fracturing. Capillary invasion was not observed in this case, suggesting that the vis-cous forces were too high to be counteracted by the capillary and gravity forces. A single finger propagated vertically from the injection point, branching out at 1.3 s. A fracture formed at 2.1 s at a lower height than the previous cases and propa-gated across the upper half of the cell. This early fracturing was likely a consequence of the high injection rate used in this case.
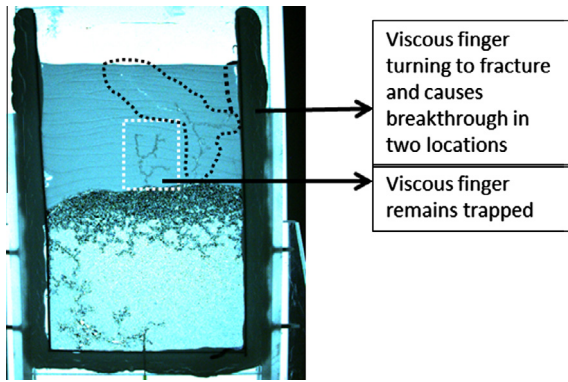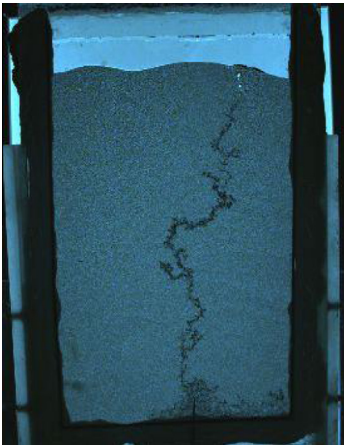
Fig. 14. Enhancement of last image in Fig. 13 (172s).

4.5. Case 5: stratified porous medium

In this experiment, we attempted to simulate the configuration of a high-permeability reservoir capped by a layer of low-permeability sediment. We filled the lower part of the cell with coarse beads (0.43–0.57 mm diameter) and the higher part with fine ones (0.10–0.20 mm diameter). We thus constructed a stratified porous medium, consisting of two layers with different permeability ranges. Air was injected at 3.8 mL/min. As can be seen in Fig. 13, a viscous finger formed within the high-permeability layer but could not penetrate the capillary barrier formed by the low-permeability layer. A considerable amount of air was trapped underneath the top layer. At 151 s, two fingers finally broke through the capillary cap, one of which reached the surface (see Fig. 14).

Table 5
The invasion patterns for two different experiments and the corresponding pressure in relation to different regimes.

Experiment	Experimental parameters	P_c (kPa)	$\Delta P_{vis} + \Delta P_{hyd}$ (kPa)
	– Q (ml/min) = 3.4 – d (mm) $\sim$ 0.32 – Pore radius (mm) $\sim$ 0.056 – k (m^2) = 2.26 $\times$ 10^{-10} – σ (mN/m) = 72	2.57	– Capillary regime (Δz = 1 cm): 0.22 – Viscous regime (Δz = 18.9 cm): 4.2
	– Q (ml/min) = 2 – d (mm) $\sim$ 0.57 – pore radius (mm) $\sim$ 0.099 – k (m^2) = 7.18 $\times$ 10^{-10} – σ (mN/m) = 72	1.45	– Capillary regime (Δz = 5 cm): 0.606 – Viscous regime (Δz = 12.3 cm): 1.49
	– Q (ml/min) = 8 – d (mm) $\sim$ 0.57 – pore radius (mm) $\sim$ 0.099 – k (m^2) = 7.18 $\times$ 10^{-10} – σ (mN/m) = 72	1.45	– Capillary regime (Δz = 1 cm): 0.19 – Viscous regime (Δz = 12.5 cm): 2.38

5. Analysis and discussion

5.1. Pressure analysis

As described in the introduction, three types of forces are in competition during drainage in the vertical cell configuration used here: the viscous forces related to the motion of the fluids, the capillary forces related to the interface between the two fluids and the forces of gravity. The capillary forces are local, while the viscous forces tend to act over a larger scale. The pressure variation across the porous medium along the z direction can be written as:

$$\Delta P = \Delta P_c + \Delta P_{vis} + \Delta P_{hyd} = \frac{2\sigma}{r} + \left(\frac{\mu_l v}{k} + \rho_l g\right)z(t) \qquad (9)$$

ΔP_c is the capillary pressure at the interface between the two phases (its expression is given above, in the case of a meniscus inside a capillary tube of radius r (Aker et al., 1998). In this expression, r is in the order of the pore radius estimated as $r_{pore} = 0.35(d_p/2)$ (Laroussi and Backer, 1979). ΔP_{vis} can be estimated from Darcy's law as $\Delta P_{vis} = \frac{\mu_l v \Delta z}{k}$. ΔP_{hyd} is the hydrostatic pressure of a vertical column of fluid (water) of length Δz.

Table 5 summarizes the invasion pattern and pressure data for three different experiments. The comparison of ΔP_c with the estimated $\Delta P_{vis} + \Delta P_{hyd}$ confirms that viscous fingering occurs when $\Delta P_{vis} + \Delta P_{hyd} > \Delta P_c$ while capillary invasion is limited to $\Delta P_{vis} + \Delta P_{hyd} < \Delta P_c$. The length Δz is that of the regime, whether viscous fingering or capillary invasion, studied for each experiment. Case 4 was not included as there was no capillary invasion.

5.2. Intermittent invasion process

For each experimental run, we observed that the invasion process was not continuous but occurred in bursts. In order to have a better grasp of this phenomenon, we tried to slow down the dynamics of the bursts. We injected air at a slow rate of 0.5 mL/min into a water-saturated cell filled with 1 mm beads. The estimated permeability was 2.2×10^{-9} m^2 and the capillary number at the injection point was 7.27×10^{-5}. With this set-up, individual bursts were easily distinguished from the preceding and following ones. Fig. 15 displays a series of successive bursts. Each image shows an individual burst at the time it appears. For example the first burst (second image) occurred after one second of injection. A period of inactivity of 1 s separated the first and the second burst (third image). Note that after the second burst, water partially reinvaded the space previously invaded during the first burst, closing the air channel near the needle and temporarily entrapping the air above. During the following bursts, this cycle of re-opening and closing of the air channel near the needle was repeated (4th to 6th pictures in Fig. 15).

Similar bursting events were previously observed and statistically characterized in a horizontal configuration (Crandall et al., 2009). Holtzman and Juanes (2010) provided a possible explanation of this phenomenon. Their pore-scale numerical simulations showed that before a burst, the air injection causes the capillary pressure to increase until it exceeds the local entry pressure and the invasion starts. In response to the invasion, the water pressure increases locally, decreasing the capillary pressure and temporarily stopping the invasion. During this period of inactivity, the excess water pressure dissipates and air pressure starts increasing again in the invaded pores due to continuous air injection. Thus the capillary pressure increases again, setting the conditions for a new burst cycle.

5.3. Fractal dimension number analysis

The fractal dimension of the invaded region was calculated for the individual bursts of each experimental run and the results are shown in Figs. 16 and 17. The fractal dimension number is used in addition to visual observation to distinguish between the regimes. We observed average fractal dimensions of 1.65 for capillary invasion bursts, 1.46 for viscous fingering and 1.25 for
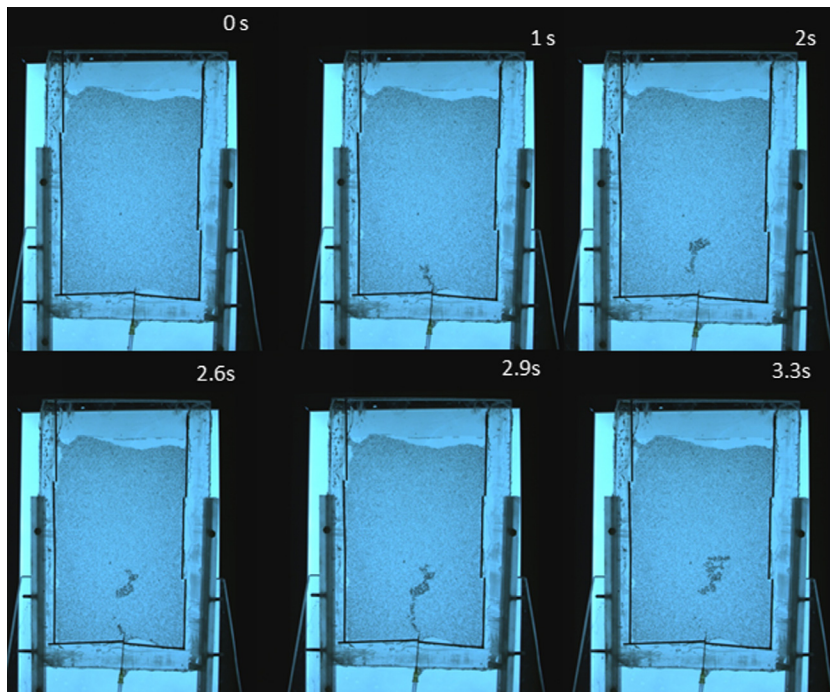

Fig. 15. Invasion pattern for 1 mm beads with injection rate = 0.5 mL/min.
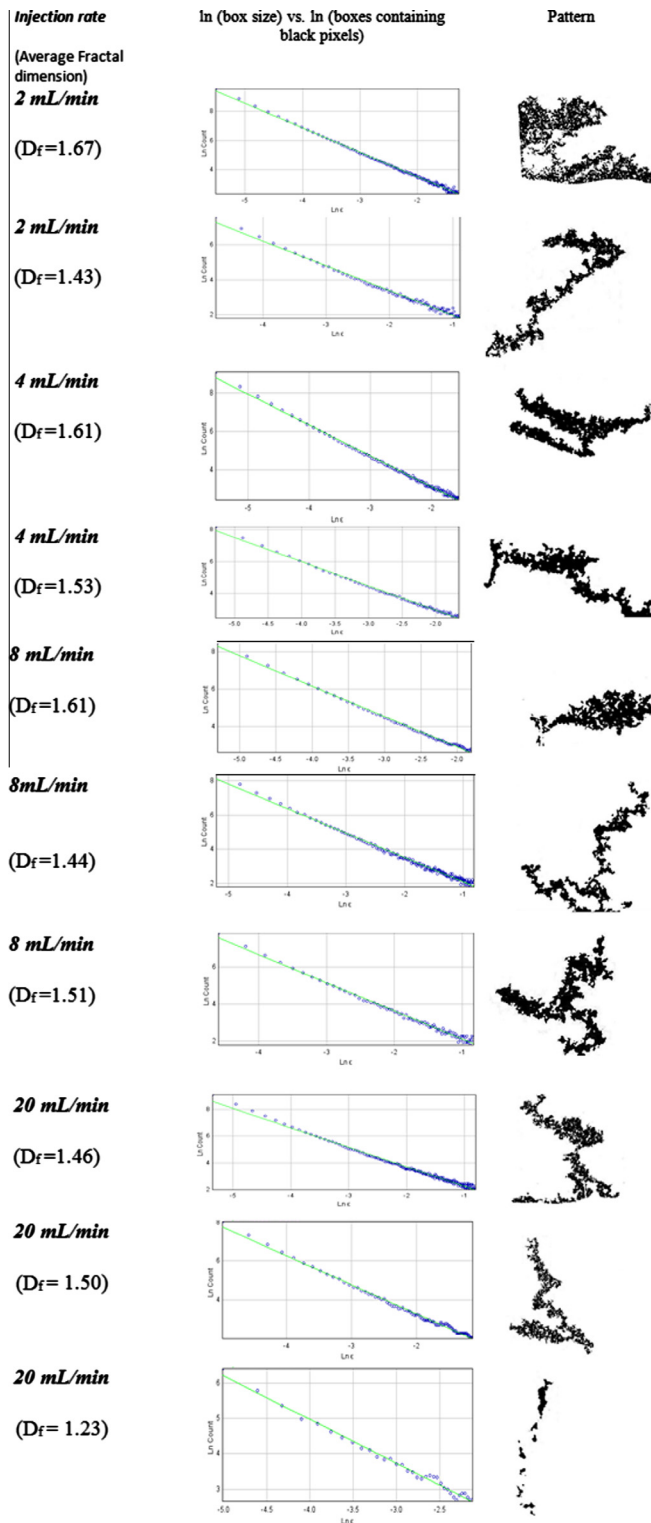
Injection rate (Average Fractal dimension)	ln (box size) vs. ln (boxes containing black pixels)	Pattern
2 mL/min (Df=1.67)		
2 mL/min (Df=1.43)		
4 mL/min (Df=1.61)		
4 mL/min (Df=1.53)		
8 mL/min (Df=1.61)		
8mL/min (Df=1.44)		
8 mL/min (Df=1.51)		
20 mL/min (Df=1.46)		
20 mL/min (Df= 1.50)		
20 mL/min (Df= 1.23)		

Fig. 16. Fractal dimension numbers and invasion patterns for experimental runs on 0.57–0.70 mm beads.

Injection rate (Average Fractal dimension)	ln (box size) vs. ln (boxes containing black pixels)	Pattern
3.4 mL/min (Df= 1.70)		
3.4 mL/min (Df=1.37)		
3.4 mL/min (Df=1.37)		
3.4 mL/min (Df=1.24)		
4 mL/min (Df=1.64)		
8 mL/min (Df=1.64)		
8 mL/min (Df=1.56)		
8 mL/min (Df=1.27)		

Fig. 17. Fractal dimension numbers and invasion patterns for experimental runs on 0.32–0.43 mm beads.

Table 6
Number of images analyzed for each flow regime and Fractal dimension number for the three regimes.

	Number of images	Fractal dimension range (average)
Capillary invasion	6	1.61–1.70 (1.645)
Viscous fingering	9	1.37–1.56 (1.46)
Fracture	3	1.23–1.27 (1.25)

fracture as summarized in Table 6. These values are slightly lower than those previously found by Holtzman and Juanes (2010); 1.82, 1.65 and 1.28 respectively. Even though the interval between our average fractal dimension numbers of capillary invasion and viscous fingering is similar to theirs (0.19 in comparison to 0.17), the discrepancy in the values may be explained by differences in configurations: namely, 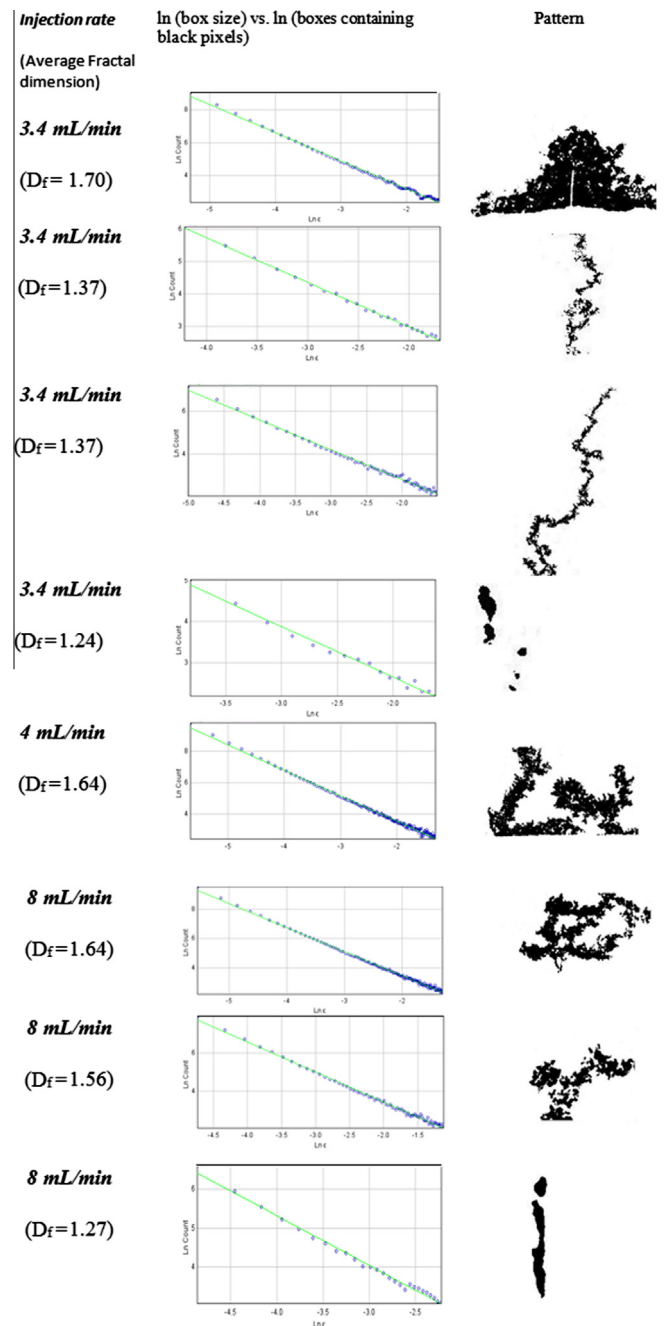vertical rectangular cell with an injection point at the bottom and gravity packing of solid particles in our work, horizontal circular cell with a central radial injection and the solid particles compressed using an externally applied normal stress in the work of Holtzman and Juanes (2010).
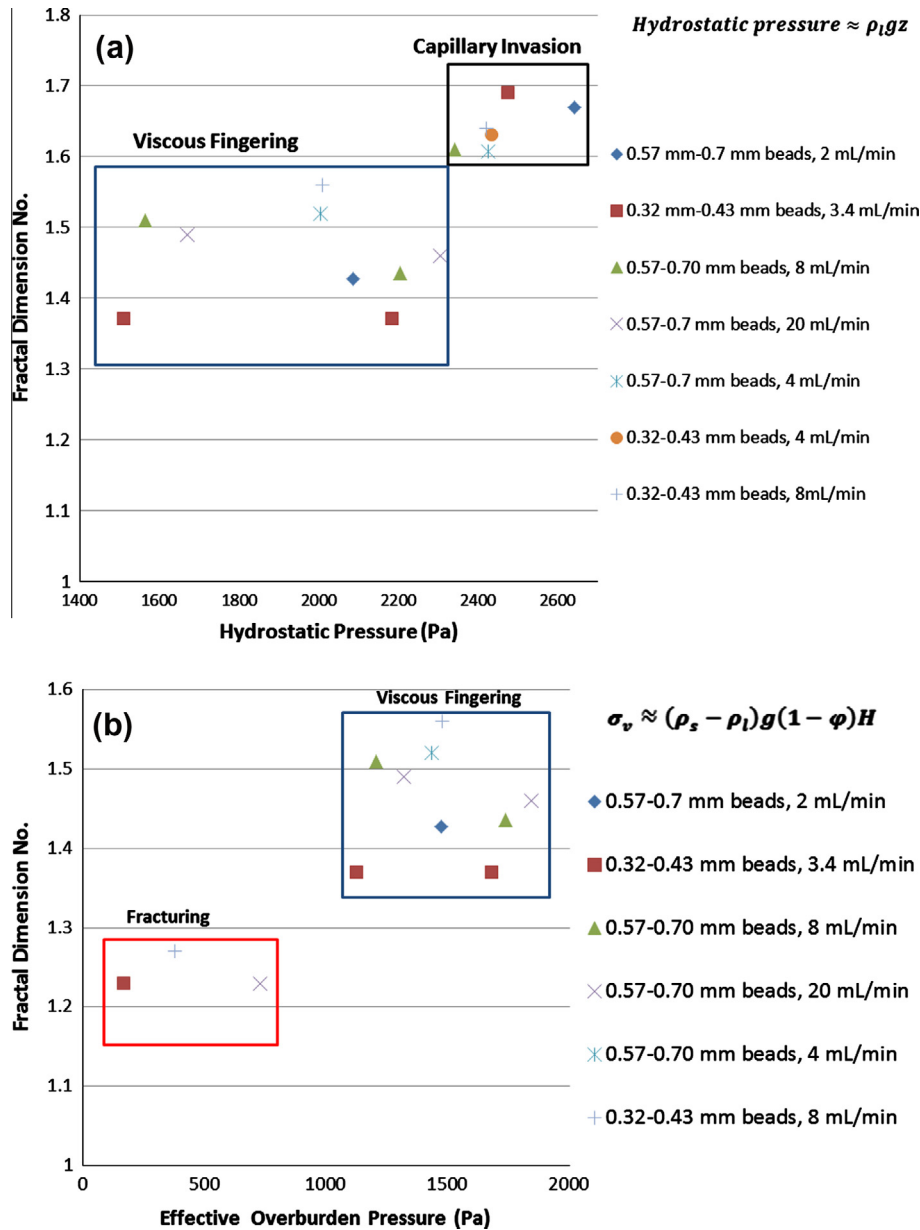
Fig. 18. (a) Hydrostatic pressure against fractal dimension showing transition between capillary invasion and viscous fingering, (b) effective overburden pressure against fractal dimension number showing the transition between viscous fingering and fracturing.

5.4. Effect of fluid and overburden pressures on Invasion Pattern

Our observations demonstrated that the invasion pattern changed with the vertical position in the Hele-Shaw cell, suggesting that fluid and overburden pressures affected the invasion process. In most experiments, capillary invasion initially occurred at the injection point and was followed by viscous fingering and fracturing at different heights of the cell. However when the capillary number was sufficiently high, the capillary invasion step was not observed. Fig. 18a shows that capillary invasion and viscous fingering occurred in different fluid pressure ranges (1512–2305 Pa for viscous fingering and 2340–2640 Pa for capillary invasion), with the hydrostatic pressure calculated using Eq. (8). The onset of fracturing was controlled by the effective overburden pressure as demonstrated in Fig. 18b. We estimated the effective overburden pressure using Eq. (7) and noted that fracturing only took place when the effective overburden pressure was lower than 900 Pa,

towards the top of the cell. At higher overburden pressure, viscous fingering occurs because the critical pressure for bead displacement is not overcome.

6. Conclusions

This work studied drainage and crossover between capillary invasion, viscous fingering and fracturing in a vertical Hele-shaw cell that has an injection point at the center of the bottom of the cell. The Hele-shaw cell was filled with glass microbeads and was saturated by water. Air was injected to displace the wetting water phase. This study differs from previous ones mainly by the single injection point and by taking into account the gravity effect on the transition between the drainage invasion regimes. The invasion was seen to happen in bursts. These invasion bursts were related to a competition between capillary and entry pressures on

one hand, between entry pressure and viscous effects on the other, and between overburden stress and entry pressure on the other. It was shown that the three regimes (capillary invasion, viscous fingering and fracturing) could be visualized within the same drainage experiment, but at different heights, emphasizing the effect of the overburden stress and the water hydrostatic pressure on the observed invasion. Gravity forces constituting the hydrostatic pressure and overburden stress were shown to have a stabilizing effect on the invasion pattern. Fractal dimension numbers were determined for the intermittent invasion patterns corresponding to the three drainage regimes, and results showed fractal dimension numbers of 1.65, 1.46 and 1.25 for capillary invasion, viscous fingering and fracturing respectively. Additionally, no capillary invasion was visualized at high capillary number at the injection point.

Acknowledgements

References

Aker, E., Maloy, K., Hansen, A., 1998. Simulating temporal evolution of pressure in two-phase flow in porous media. Phys. Rev. E 58, 2217–2226.

Chun, B., Wilkinson, G., 1995. Interfacial tension in high pressure carbon dioxide mixtures. Ind. Eng. Chem. Res. 34, 4371–4377.

Crandall, D., Ahmadi, G., Ferer, M., Smith, D.H., 2009. Distribution and occurrence of localized-bursts in two-phase flow through porous media. Physica A 388, 574–584.

EPIX Inc. (n.d.). PIXCI Imaging Boards. Retrieved 2011. <http://www.epixinc.com/products/xcap.htm>.

Fauria, K.E., Rempel, A.W., 2011. Gas invasion into water-saturated, unconsolidated porous media: Implications for gas hydrate reservoirs. Earth Planet. Sci. Lett. 312, 188–193.

Ghaderi, S., Keith, D.M., Leonenko, Y., 2009. Feasibility of injecting large volumes of CO_2 into aquifers. Energy Procedia 1, 3113–3120.

Holloway, S., 2005. Underground sequestration of carbon dioxide – a viable greenhouse gas mitigation option. Energy 30, 2318–2333.

Holtzman, R., Juanes, R., 2010. Crossover from fingering to fracturing in deformable disordered media. APS Phys. Rev. E 82, 1–5.

Holtzman, R., Szulczewski, M., Juanes, R., 2012. Capillary fracturing in granular media. Phys. Rev. Lett. 108, 1–4.

Homsy, G.M., 1987. Viscous fingering in porous media. Annu. Rev. Fluid Mech. 19, 271–311.

ImageJ. (n.d.). Retrieved 2012. <http://imagej.nih.gov/ij/plugins/fraclac/FLHelp/Introduction.htm#software>.

IPCC special report on carbon capture and storage. 2005. (Working Group 3). Retrieved April 2011. <http://www.ipcc.ch/>.

Jiao, C., Maxworthy, T., 2008. An experimental study of miscible displacement with gravity-override and viscosity-contrast in a Hele Shaw cell. Exp. Fluids 44, 781–794.

Koike, A., Tomozawa, M., 2007. IR investigation of density changes of silica glass and soda-lime. J. Non. Crys. Solids 353, 2318–2327.

Kopf-Sill, A.R., Homsy, G.M., 1988. Nonlinear unstable viscous fingers in Hele-Shaw flows. 1. Experiments. Phys. Fluids 31, 242–249.

Laroussi, C., Backer, L.W., 1979. Relations between geometrical properties of glass beads media and their main hysteresis loops. Soil Sci. Soc. Am. J. 43, 646–650.

Lemmon, E., Huber, M.L., McLinden, M., 2007. Refprop Version 8.0 based on NIST Standard Reference. Database 23.

Løvoll, G., Meheust, Y., Maloy, K.J., Aker, E., Schmittbuhl, J., 2005. Competition of gravity, capillary and viscous forces during drainage in a two-dimensional porous medium, a pore study. Energy 30, 861–872.

Mota, M., Teixeira, J.A., Bowen, W.R., Yelshin, A., 2001. Binary spherical particle mixed beds: porosity and permeability relationship measurement. Trans. Filt. Soc. 1, 101–106.

Saffman, P., Taylor, G., 1958. The penetration of a fluid into a porous medium or Hele-Shaw cell containing a more viscous liquid. Proc. Roy. Soc. Lond., 312–329.

Smirnov, N., Nikitin, V., Maximenko, A., Legros, M.T., 2005. Instability and mixing flux in frontal displacement of viscous fluids. Phys. Fluids 17, 084102.

Sony Inc. (n.d.). Sony: XCL U1000c. Retrieved 2011. <http://pro.sony.com/bbsc/ssr/cat-industrialcameras/cat-cameralink/product-XCL5005CR/>.

Zhang, C., Oostrom, C.M., Wiestsma, T.W., Grate, J.W., Warner, M.G., 2011. Influence of viscous and capillary forces on immiscible fluid displacement: pore-scale experimental study in a water-wet micromodel demonstrating viscous and capillary fingering. Energy Fuels 25, 3493–3505.